

## N O T I C E

THIS DOCUMENT HAS BEEN REPRODUCED FROM  
MICROFICHE. ALTHOUGH IT IS RECOGNIZED THAT  
CERTAIN PORTIONS ARE ILLEGIBLE, IT IS BEING RELEASED  
IN THE INTEREST OF MAKING AVAILABLE AS MUCH  
INFORMATION AS POSSIBLE

(NASA-TM-81987) THE FORMATION OF ARCS IN  
THE DYNAMIC SPECTRA OF JOVIAN DECAMETER  
BURSTS (NASA) 34 p HC A03/MF A01 CSCL 03B

N81-12966

Unclas  
G3/91 39828



## Technical Memorandum 81987

# The Formation of Arcs in the Dynamic Spectra of Jovian Decameter Bursts

Melvyn L. Goldstein and  
James R. Thieman

AUGUST 1980

National Aeronautics and  
Space Administration

Goddard Space Flight Center  
Greenbelt, Maryland 20771



**THE FORMATION OF ARCS IN THE DYNAMIC SPECTRA OF JOVIAN DECAMETER BURSTS**

**Melvyn L. Goldstein**  
**Laboratory for Extraterrestrial Physics, NASA Goddard Space Flight Center**  
**Greenbelt, Maryland 20771**

**James R. Thieman**  
**ORI, Inc., Space Systems Analysis Division**  
**Silver Spring, Maryland 20910**

**SUBMITTED TO: Journal of Geophysical Research**

Abstract. A model is presented that can account for several features of the dynamic spectral arcs observed at decameter wavelengths by the planetary radio astronomy experiment on Voyagers 1 and 2. We first show that refraction of an extraordinary mode wave initially excited nearly orthogonal to the local magnetic field is significantly influenced by the local plasma density, being greater the higher the density. We assume that the source of the decameter radiation lies along the  $L = 6$  flux tube and that the highest frequencies are produced at the lowest altitudes, where both the plasma density and magnetic field gradients are largest. We further assume that the decameter radiation is emitted into a thin conical sheet, consistent with both observation and theory. In the model the emission cone angle of the sheet is chosen to vary with frequency so that it is relatively small at both high and low frequencies, but approximately  $80^\circ$  at intermediate frequencies. The resulting emission pattern as seen by a distant observer is shown to resemble the observed arc pattern. The model is compared and contrasted with examples of Voyager radio data.

## 1. Introduction

One of the most dramatic discoveries made by the Voyager 1 and 2 planetary radio astronomy (PRA) experiment has been the observation that the dynamic spectra of Jupiter's decameter radiation is organized into a series of arc-like patterns (Warwick et al. [1979a, b]; for a review of observations of arcs, see Boischot et al. [this issue]). Motivated by these observations, we have developed a model for the formation of spectral arcs that is basically a geometrical consequence of the multipole magnetic field models constructed from the Pioneer 11 magnetometer experiments [Acuña and Ness, 1976; Smith et al., 1976]. The model is compared with observations of both 'greater' and 'lesser' arcs.

Because the spectral arc model is basically a geometrical construction, the following discussion is presented without explicit reference to particular theories for the generation of decameter radiation. There are, however, several general requirements that we assume about the source of the radiation. The first of these is that the radio waves are excited by kilovolt electrons. Evidence for large fluxes of electrons in this energy range has been reported [e.g., Fillius, 1976; Krimigis et al., 1979; Coroniti et al., 1980]. Second, we assume that the radiation is excited just above the right-hand cutoff frequency

$$\omega_R = \frac{1}{2} |\Omega_e| [1 + (1 + 4\omega_{pe}^2/\Omega_e^2)^{1/2}]$$

where  $\omega_{pe} = \sqrt{4\pi Ne^2/m}$  is the electron plasma frequency and  $\Omega_e = -|e|B/mc$  is the local electron gyrofrequency ( $m$  is the electron mass). Consequently, the radiation can directly escape the Jovian magnetosphere without encountering the stop zone that lies between the upper-hybrid and right-hand cutoff

PRECEDING PAGE BLANK NOT FILMED

frequencies. Third, we assume that the source of the radiation lies somewhere above the Jovian ionosphere, on field lines that are part of the global magnetic field approximately described by the octupole models referenced above. A rather different viewpoint is espoused by Warwick [this issue], who attributes the source locations to local anomalies in the field, undetectable by the Pioneer 11 experiments. We do not restrict the model to stably trapped fluxes of energetic electrons because recent radio observations indicate that even the Io-phase-independent radiation often exceeds 28 MHz, the maximum gyrofrequency accessible to stably trapped electrons, and sometimes reaches 34 MHz [Barrow and Desch, 1980]. That the Io-independent component is observed at such high frequencies indicates that if trapped electrons are involved, the maximum magnetic field in the southern hemisphere must exceed the 10.7 G maximum cloud-top field predicted by the octupole magnetic field models. Alternatively, the observation implies that both the Io-phase-independent as well as the Io-phase-dependent components are generated by electrons precipitating into the northern hemisphere ionosphere (where the magnetic field strength reaches 14 G).

Virtually all emission mechanisms that have thus far been proposed for generating the decameter radiation (see Smith [1976] for a review) predict that the radiation will be emitted into a thin conical sheet of half angle  $\Psi$ . The magnitude of  $\Psi$  will be determined by the interplay between the angular dependence of the growth rate of whatever plasma instability produces the radiation and the amount of refraction experienced by the radiation as it propagates out of the source. The refraction is primarily determined by the magnitudes of the index of refraction  $n \equiv kc/\omega$ , the group velocity  $v_g$  ( $v_g \equiv \partial\omega/\partial k$ ) as well as the spatial gradients and magnitudes of both the magnetic field  $B$  and electron density  $N$ . When the radiation is generated very close to

$\omega_R$ , both  $v_g/c$  and  $n$  are much less than unity [Goldstein and Eviatar, 1979]. Furthermore, especially at the highest frequencies, the spatial gradients and magnitudes of  $\underline{B}$  and  $N$  are large. Consequently, as we show below, the radiation will be refracted more at high frequencies than at lower ones.

Although we speak of the emission pattern as being conical, there is no a priori reason to expect that  $\Psi$  will be the same in all directions. Asymmetries in the magnetic field and in the local gradients can easily cause  $\Psi$  to vary with azimuth about  $\underline{B}$ .

## 2. Dynamic Spectral Arcs

Warwick et al. [1979b] have pointed out that an arclike pattern will result from any emission mechanism that predicts beaming of the decameter radiation into thin conical sheets. The exact nature of the observed emission pattern, however, depends on the location of the source and on  $\Psi$  at that location. Various alternative approaches to constructing arc patterns are discussed by Pearce [this issue] and Staelin [this issue].

As an example of the type of dynamic spectrum that results from assuming that the decameter radiation is beamed into thin conical sheets, let us consider the following example. Let the source be located on the  $L = 6$  flux tube and assume that  $\Psi$  is nearly  $80^\circ$  at all frequencies. The resulting pattern is shown in Figure 1. In constructing the figure we used the O4 octupole magnetic field model to calculate the intersection with the ecliptic plane of a conical sheet with constant half-angle  $\Psi = 79^\circ$  along magnetic field lines from 1 MHz to the gyrofrequency at the cloud tops. The calculation was done at  $20^\circ$  intervals of longitude.

In the construction of Figure 1 and in similar plots discussed below, it is

assumed that the radiation mechanism produces discrete arcs. The model we present addresses only the question of why the dynamic spectra are curved into arclike patterns. The equally important question of why the pattern is discrete is a separate one that is beyond the scope of this discussion. However, two models have been suggested for producing the discreteness. In the first, Gurnett and Goertz [1980] attribute it to multiple reflections of the current-carrying Alfvén waves that propagate between Io and the Jovian ionosphere [Neubauer, 1980]. Our model for producing curved arcs is compatible with theirs for producing discrete ones. The second suggestion by Boischot and Aubier [this issue] is that destructive interference between neighboring flux tubes gives rise to the observed pattern. We expect that this idea is also compatible with the model we present.

The separate panels in Figure 1 show the frequency versus longitude for each of the two sides of the conical sheets separately as 'Vertex Early' and 'Vertex Late' arcs. In addition, the patterns from the northern and southern hemispheres have been separated. The discrete dots in the plots result from moving the apex of the radiating conical sheet along the field line in 1-MHz (0.36 G) increments. (The occasional discontinuities result from failures of an interpolation algorithm used to find the 1 MHz increments.)

The calculation of the longitudes of the intersection of the conical sheet with the Jovigraphic plane is carried out precisely as was done by Goldstein et al. [1979]. In fact, if the plots in that paper of  $\nu$  (redefined below) versus central meridian longitude (CML) at several frequencies were redrawn as frequency versus CML, arclike patterns essentially identical to those in Figure 1 result. The pattern in Figure 1 is calculated by noting that the cone of emission intersects the equatorial plane along a curve whose asymptotes are two straight lines which in turn meet at an angle  $2\mu$  where  $\mu =$



$\arctan/(\tan^2 \gamma \cos^2 i - \sin^2 i)$  and  $i = \arccos(B_0/B)$  [Goldreich and Lynden-Bell, 1969].  $B_0$  is the projection of  $B$  onto the Jovigraphic equatorial plane. If  $B_\phi$  is the  $\phi$  component of  $B$  at the apex of the cone (in a right-handed spherical coordinate system), then the longitude toward which  $B_0$  points is  $\lambda' = \phi \pm \beta$ , where  $\beta = \arcsin(B_\phi/B_0)$  and the plus sign and minus signs refer to the southern hemisphere and northern hemisphere, respectively. The source locations are then  $\Lambda(\pm) = \lambda' \pm \mu$ , where here the plus and minus denote the two sides of the emission cone.

Several things are readily apparent from Figure 1. First, this pattern shows very little curvature and does not resemble arcs at all. Second, lines in the panels originating from opposite sides of the same emission cone at  $\Lambda(\pm)$  tend to curve away from each other especially at low frequencies. This is illustrated in the figure by darkening the pair of curves ( $\Lambda(\pm)$ ) arising from the northern hemisphere trace of the emission cone whose apex passes along that field line that crosses the equatorial plane at  $r = 5.95$  Jovian radii and  $\lambda = 200^\circ$  longitude at the equator (all longitudes are given in system III-1965). The limited curvature results because as the apex of the emission cone moves from high frequencies near the ionosphere to lower frequencies at greater distances from Jupiter, the lines of force tend to curve increasingly toward the equatorial plane, and thus  $\mu$  and the separation between  $\Lambda(+)$  and  $\Lambda(-)$  increase. When the apex of the emission cone is near  $\lambda = 200^\circ$ , we assign the  $\Lambda(+)$  'arcs' to source A (main source) and the  $\Lambda(-)$  side of the cone to source B (early source), as was done by Goldstein et al. [1979]. The observed arcs (cf. Boischot et al. [this issue] and Figures 6 and 11 below) in the Source A and B regions have considerably more curvature than those shown in Figure 1. Moreover, the observed curvature is in the opposite sense.

To progress further it is necessary to relax one or more of the constraints

imposed on the construction of Figure 1. One possibility is to allow the source to be placed somewhere closer to  $L = 2$ . Doing so increases the curvature of some of the 'arcs', especially if  $\Psi$  is also decreased, and at some longitudes will produce arcs with approximately the observed curvature. There will, however, be a problem with the range of allowed frequencies if one retains the assumption that  $\omega > \omega_R$ , because the gyrofrequencies reached by lines of force on the  $L = 2$  flux tube never exceed 36 MHz and are usually much less. Examples of such a calculation are shown in Figures 2 and 3. In Figure 2,  $\Psi = 79^\circ$  was retained, and only vertex early arcs produced in the northern hemisphere are shown. Again, the pattern near  $100^\circ$  CML that should be related to the early source exhibits little curvature, and the little that is evident is still in the opposite sense to that observed.

In Figure 3 we illustrate the effect of using a small ( $45^\circ$ ) value for  $\Psi$ , first for the  $L = 2$  flux tube in the northern hemisphere (top pairs of panels), and then for  $L = 6$  in the lower pairs of panels. The almost complete absence of any recognizable arc pattern in the  $L = 6$  calculations arises because the emission cone angle is so small that the emission pattern more often than not completely misses the equatorial plane. Furthermore, if  $\Psi = 45^\circ$  at all frequencies, then the hypothesis must be abandoned that the early and main sources, which are separated in CML by  $90^\circ$  or more, reflect two sides of a single conical sheet of radiation.

Before describing a particular model that does produce curved dynamic spectra, let us reconsider some aspects of refraction of the extraordinary mode. Goldstein and Eviatar [1979] found that refraction introduces a frequency dependence into  $\Psi$  that caused  $\Psi$  to decrease with decreasing frequency. Such a functional dependence will not, however, produce true 'arc' patterns with a well developed 'vertex frequency'  $f_v$ . In obtaining the result that  $\Psi$

was a monotonically decreasing function of frequency, it was assumed that the ambient electron density  $N$  was a constant equal to  $100 \text{ cm}^{-3}$  everywhere along the flux tube, even near the cloud tops. More appropriate values, as determined from radio occultation measurements [Fjeldbo et al., 1976] range from a few hundred to  $3 \times 10^3$  electrons/cm<sup>3</sup>. By increasing the density the estimated refraction is also increased, as illustrated in Figure 4.

Figure 4 is calculated by using the approximate formula for  $\Delta\epsilon$  derived in Goldstein and Eviatar [1979], where  $\Delta\epsilon$  is the integrated change in  $\epsilon$  (the angle between  $\underline{k}$  and  $\underline{B}$ ) along the ray path and is given by

$$\Delta\epsilon = \int_0^S ds \frac{H(s)}{n(v_g/c)B} \frac{dB(s)}{ds} \quad (1)$$

with

$$H = \frac{(1 - v)[1 - v(1 - n^2 - 2v)] - n^2}{2(1 - v) - n^2 - (\omega^2/n_e^2) \sin^2 \epsilon}$$

$$v = \omega_{pe}^2/\omega^2$$

and  $n$  is found from the Appleton-Hartree dispersion relation [Stix, 1962].  $S$  is defined to be the distance along the ray path to the point where  $n = 1$ ,  $v_g/c = 1$ , and the integrand of (1) is nearly zero. (The integration is also halted if  $\Delta\epsilon$  becomes so large that the emerging ray can no longer intersect the equatorial plane.) Many of the limitations of this approximate calculation are discussed in Goldstein and Eviatar [1979].

Assuming an ambient electron density of  $1.6 \times 10^3 \text{ cm}^{-3}$ , radiation excited near the ionosphere experiences strong refraction. The resulting emission cone angles are close to  $65^\circ$ . Further along the line of force where the density is only a few hundred electrons per cm<sup>3</sup>, the refraction will be only a

few degrees, yielding  $\Psi = 80^\circ$  as found before. At yet greater distances and lower frequencies the effective value of  $\Psi$  should again decrease either because the conical sheet becomes thicker and the emission cone becomes more filled, or because the growth rate of the instability maximizes at smaller values of  $f$ .

The calculation shown in Figure 4 is meant primarily to motivate the model discussed below. Although there will be longitudes at which radiation at 23 MHz is produced in a  $1.6 \times 10^8/\text{cm}^3$  plasma, the value of  $N$  at a given frequency varies with longitude. Therefore we do not present a complete calculation of these effects, primarily because of the inadequacies inherent in our approximate ray tracing calculation, but also because of the necessity of incorporating a global model of electron density in the Jovian magnetosphere from the inner edge of the  $10^8$  plasma torus to the ionosphere.

Because we wish to investigate the types of variations in  $\Psi$  with frequency that are consistent with the observed dynamic spectra, we have developed a simple model that is consistent with the refraction estimates discussed above. We define a function  $\Psi(f)$  with the property that near the cloud tops  $\Psi(f) = \Psi_{\min}$ .  $\Psi(f)$  then increases as  $f$  decreases along the flux tube, reaching a maximum of  $\Psi(f) = 80^\circ$  at  $f_v = (f_{\max} + f_{\min})/w$ , where  $f_{\max}$  is the gyrofrequency at the ionosphere for a field line in the hemisphere of interest,  $f_{\min} = 1$  MHz is the minimum frequency considered, and  $w$  is taken to be 3 except when attempting to model the early source where  $w = 2$  was used. At frequencies below  $f_v$ ,  $\Psi(f)$  decreases to  $\Psi_{\min}$  at  $f_{\min}$ . An example of 'arcs' produced by this model is shown in Figure 5, where  $\Psi_{\min} = 65^\circ$  and  $\Psi(f)$  is defined by

$$\gamma(f) = 80^\circ \sin \left( \frac{\pi}{2} \right) \left( \frac{f_{\max} - (1-a)f - af_v}{f_{\max} - f_v} \right)$$

$$f \geq f_v$$

$$\gamma(f) = 80^\circ \sin \left( \frac{\pi}{2} \right) \left( \frac{(1-a)f + af_v - 1}{f_v - 1} \right)$$

$$f \leq f_v$$

(2)

where  $f$  is in MHz. The coefficient  $a$  is defined so that  $\gamma(f) = \gamma_{\min}$  at both  $f = f_{\max}$  and  $f = f_{\min}$ . For  $\gamma_{\min} = 65^\circ$ ,  $a = 0.6038$ . The arcs resulting from this model do have the correct sense of curvature if sources A and B are assumed to arise from beaming into two sides of the same conical sheet with vertex near  $200^\circ$ . As in Figure 1 the same pair of curves ( $\pm$ ) are darkened.

For comparison, Figure 6 superimposes the modeled arcs on an Io-dependent A source event recorded by Voyager 2 on July 6-7, 1979, as well as an Io-independent source A and Io-dependent source C event observed July 3, 1979. The curvature of the model arcs follows the observed arcs quite well. This is especially clear for the largest Io-A arc, which reaches a frequency of 36 MHz at a CML of approximately  $240^\circ$ . The other arcs that are evident in the two panels are all similar in curvature to the largest arc so that they are also reasonably well modeled. Although the frequency extent of the arcs in the source A and C regions is observed to vary from one rotation to the next, the curvature of these arcs remains quite constant. Further examples of this can be found in Figure 4a of Boischoat et al. [this issue]. In Figure 6 the highest frequency ( $\approx 39$  MHz) is found near  $\Lambda(+) = 180^\circ$  CML. In contrast, the maximum frequency of the observed arcs is found closer to  $240^\circ$ . The Io-dependent C arcs agree in both curvature and upper frequency cutoff with the

model except for the greatest arc that ends at 34 MHz near 300° CML. We return below to a discussion of the large disagreement of the high frequency limits. Note also that the present construction ascribes source C to the northern hemisphere, as implied by the PRA experiment's polarization determinations.

One additional consequence of this model is indicated in Figure 5. The asterisks (\*) along the high frequency ends of the arcs delimit the highest frequencies that can be excited by stably trapped electrons (assuming, of course, that the O4 magnetic field model is accurate). Thus arcs arising from trapped electrons as assumed for the Io-independent sources by Goldstein et al. [1979] and Goldstein and Eviatar [1979] should be limited primarily to frequencies at and below the asterisks.

Although there is nothing particularly unique about the choice of (2), it does have the property that arcs at different longitudes are approximately homologous in the sense defined by Warwick et al. [1979b]. One should keep in mind, however, that the general prevalence of homologous arcs in the data has not yet been investigated. We demonstrate that the arcs shown in Figure 5 are homologous by defining a dimensionless frequency  $\bar{f} = (f - 1)/(f_{\max} - 1)$  and a dimensionless longitude  $\bar{\lambda} = (\lambda_{\max} - \lambda)/(\lambda_{\max} - \lambda_{\min})$ , where  $\lambda_{\max}$  is the longitude of the vertex frequency of the arc and  $\lambda_{\min}$  is the smallest longitude along the arc (typically at either  $f = f_{\max}$  or  $f = 1$  MHz). Three arcs chosen at random (the dashed curves in Figure 5) are replotted in these dimensionless units in Figure 7. The apexes of these three emission cones lie on field lines which cross the magnetic equator at  $\lambda = 160^\circ$ ,  $220^\circ$ , and  $330^\circ$ . Note that in Figure 7 the vertices of these arcs lie at  $\bar{f} = 0.5$  because the vertex frequency was defined to be  $(f_{\max} + 1)/3$ . The homologous arcs plotted by Warwick et al. [1979b] have vertex frequencies that are a smaller fraction of

the maximum frequency, as is the case with many vertex late arcs, so that the homologous arc plots differ in detail.

We have also tried varying  $\psi_{\min}$ , thereby attempting to match a little better the variety of arc patterns seen in the data. For example, if  $\psi_{\min} = 45^\circ$  the pattern has very sharp curvature that at some longitudes does not intersect the Jovigraphic equatorial plane, as illustrated in Figure 8. These arcs are reminiscent of the lesser arcs described by Boischot et al. [this issue]. Figure 9 compares the vertex late arc pattern to the lesser arcs observed by Voyager 2 on July 7, 1979. These lesser arcs were observed immediately following the Io-dependent source A event shown in the top panel of Figure 6. The modeled and observed curvatures and vertex frequencies are in reasonable agreement, although the maximum frequency limits of the arcs are not. The lesser arcs have the same sense of curvature as the great arc source A event which occurred just prior to them.

Careful examination of the Voyager records reveals several instances where the great arc events in the source A and C longitudes appear to merge with the lesser arcs of the same curvature observed at low longitudes, suggesting that they are all part of the same  $L = 6$  family. Similarly, the vertex early source B great arcs often appear to evolve into the vertex-early lesser arcs observed in the source A and C longitudes. Recall that in Figure 6  $\psi_{\min} = 65^\circ$ , while in Figure 9  $45^\circ$  was used. Thus in modeling the continuous evolution of the arc family the minimum cone angle should probably vary with longitude, which is consistent with the refraction hypothesis suggested above. Differences in ionospheric density at a given frequency, together with possible local time effects [Alexander et al., this issue], could in principle cause the observed variations.

Although some of the observed arcs have curvatures consistent with relatively small values of  $\psi_{\min}$ , the Io-B Source can only be modeled if  $\psi_{\min}$  is

physical explanation which is only suggested by the azimuthal variation of B. A more serious difficulty is the disagreement between predicted and observed longitudes of the high frequency cutoffs.

Acknowledgments. M. L. G. would like to express his appreciation to the members of the Astronomy Department of the University of Florida for their gracious hospitality while some of this research was in progress. The work of J. R. T. has been supported by NASA contract NAS 5-25932.

PRECEDING PAGE BLANK NOT FILMED



## References

- Acuña, M. H., and N. F. Ness, Results from the GSFC fluxgate magnetometer on Pioneer 11, Jupiter, edited by T. Gehrels, p. 830, University of Arizona Press, Tucson, 1976.
- Alexander, J. K., T. D. Carr, J. R. Thieman, J. J. Schauble, and A. C. Riddle, Synoptic observations of Jupiter's radio emissions: Average statistical properties observed by Voyager, J. Geophys. Res., this issue.
- Barrow, C. H., and M. D. Desch, Non-Io decametric radiation from Jupiter at frequencies above 30 MHz, Astron. Astrophys., in press, 1980.
- Boischot, A., and M. Aubier, The Jovian decametric arcs as an interference pattern, J. Geophys. Res., this issue.
- Boischot, A., A. Lecacheux, M. L. Kaiser, M. D. Desch, J. K. Alexander, and J. W. Warwick, Radio Jupiter after Voyager: An overview of the planetary radio astronomy observations, J. Geophys. Res., this issue.
- Coroniti, F. V., F. L. Scarf, C. F. Kennel, W. S. Kurth, and D. A. Gurnett, Detection of Jovian whistler mode chorus: Implications for the Io torus aurora, Geophys. Res. Lett., 7, 45, 1980.
- Fillius, W., The trapped radiation belts of Jupiter, Jupiter, edited by T. Gehrels, p. 896, University of Arizona Press, Tucson, 1976.
- Fjeldbo, G., A. Kliore, B. Seidel, D. Sweetnam, and P. Woiceshyn, The Pioneer 11 radio occultation measurements of the Jovian ionosphere, Jupiter, edited by T. Gehrels, University of Arizona Press, Tucson, 238, 1976.
- Goldreich, P., and D. Lynden-Bell, Io, a Jovian unipolar inductor, Astrophys. J., 156, 59, 1969.
- Goldstein, M. L., and A. Eviatar, An emission mechanism for the Io-independent Jovian decameter radiation, Astrophys. J., 230, 261, 1979.

- Goldstein, M. L., A. Eviatar, and J. R. Thieman, A beaming model of the Io-independent Jovian decameter radiation based on multipole models of the Jovian magnetic field, Astrophys. J., 229, 1186, 1979.
- Gurnett, D. A., and C. K. Goertz, Multiple Alfvén wave reflections excited by Io: Origin of the Jovian decametric arcs, J. Geophys. Res., in press, 1980.
- Krimigis, S. M., T. P. Armstrong, W. J. Arnold, C. O. Bostrom, C. Y. Fan, G. Gloeckler, L. J. Lanzerotti, E. P. Keenan, R. D. Zwickl, J. F. Carbary, and D. C. Hamilton, Hot plasma environment at Jupiter: Voyager 2 results, Science, 206, 977, 1979.
- Neubauer, F. M., Nonlinear standing Alfvén wave current system at Io: Theory, J. Geophys. Res., 85, 1171, 1980.
- Pearce, J. B., A heuristic model for Jovian decametric arcs, J. Geophys. Res., this issue.
- Smith, E. J., L. Davis, Jr., and D. E. Jones, Jupiter's magnetic field and magnetosphere, Jupiter, edited by T. Gehrels, p. 788, University of Arizona Press, Tucson, 1976.
- Smith, R. A., Models of Jovian decametric radiation, Jupiter, edited by T. Gehrels, p. 1146, University of Arizona Press, Tucson, 1976.
- Staelin, D. H., Models for the origin of Jovian decametric emission, J. Geophys. Res., this issue.
- Stix, T. H., The Theory of Plasma Waves, McGraw Hill, New York, 1962.
- Warwick, J. W., Models for decametric arcs, J. Geophys. Res., this issue.
- Warwick, J. W., J. B. Pearce, A. C. Riddle, J. K. Alexander, M. D. Desch, M. L. Kaiser, J. R. Thieman, T. D. Carr, S. Gulkis, A. Boischot, C. C. Harvey, and B. M. Pederson, Voyager 1 planetary radio astronomy observations near Jupiter, Science, 204, 995, 1979a.
- Warwick, J. W., J. B. Pearce, A. C. Riddle, J. K. Alexander, M. D. Desch, M.

L. Kaiser, J. R. Thieman, T. D. Carr, S. Gulkis, A. Boischot, Y. Leblanc,  
B. M. Pederson, and D. H. Staelin, Planetary radio astronomy observations  
from Voyager 2 near Jupiter, Science, 206, 991, 1979b.

(Received June 23, 1980;  
revised August 13, 1980;  
accepted August 15, 1980.)

## Figure Captions

Fig. 1. The predicted shapes of the arcs resulting from a hollow conical sheet of radiation centered on the  $L = 5.95$  magnetic flux tube as observed from the Jovigraphic equatorial plane. Cone orientations are computed for 1-MHz intervals in gyrofrequency (up to the maximum frequency reached by the foot of the flux tube at the ionosphere) along magnetic field lines separated  $20^\circ$  in longitude. The central meridian longitude of the observer is plotted against the frequency of the emitted radiation for a fixed cone angle of  $\gamma = 79^\circ$ . Radiation can be generated in both the northern (left panels) and southern (right panels) hemispheres. As the cones rotate with the planet the observer sees vertex-early arcs (top panels) from the leading edges and vertex-late arcs (bottom panels) from the trailing edges. The panels are broken into two longitude ranges to facilitate comparison with observed dynamic spectra. The northern hemisphere curves resulting from the emission cone whose vertex passes through  $\lambda = 200^\circ$  at the equator are darkened. These curves lie near the positions of the early and main source as discussed in the text. (The occasional discontinuities in the patterns of dots arise from failures of the interpolation algorithm to correctly locate the 1 MHz increments.)

Fig. 2. The construction is done exactly as in Figure 1 only here the  $L = 2$  flux tube has been chosen to illustrate the fact that the arc curvature is somewhat increased by moving the source to smaller  $L$  values. However, emission above 30 MHz occurs only over a very limited range of CML, and again the sense of curvature is inverted. Only the vertex-early northern hemisphere pattern is plotted.

Fig. 3. The effect of choosing a small ( $\Psi = 45^\circ$ ) but constant emission cone angle is illustrated. In the top half of the figure the  $L = 2$  flux tube was used. Vertex-early patterns are shown on the left and vertex-late patterns on the right. In the lower half of the figure the same calculation has been repeated for the  $L = 6$  flux tube. Only the northern hemisphere is shown. With  $\Psi = 45^\circ$ , emission cones originating on  $L = 6$  often do not intersect the equatorial plane. Furthermore, the resulting pattern does not even approximately resemble the observed one.

Fig. 4. The effect of varying the ambient electron density on the refraction of the unstable extraordinary wave is illustrated. In this plot  $\Psi$ , the angle between the ray vector of the wave and the local magnetic field as the ray leaves the source is plotted against  $N$ , the electron density. The calculation was done on the  $L = 6$  flux tube that crossed the equatorial plane at  $180^\circ$  CML at the northern hemisphere latitude at which  $f = 23$  MHz.

Fig. 5. Similar to Figure 1 except that  $\Psi$  was varied at each point along the flux tube according to equation (2). At both  $f_{\max}$  and  $f_{\min}$  (defined in the text)  $\Psi(f_{\max}) = \Psi(f_{\min}) \equiv \Psi_{\min} = 65^\circ$ . At the vertex frequency  $f_v$ ,  $\Psi(f_v) = 80^\circ$ . The three arcs drawn with dashed lines have been replotted in dimensionless units in Figure 7. The pair of northern hemisphere arcs drawn with solid lines arise, as in Figure 1, from the flux tube that passes through  $\lambda = 200^\circ$  at the equator. The asterisks (\*) along the high frequency ends of the arcs delimit the highest gyrofrequencies attainable by stably trapped electrons.

Fig. 6. An overlay of the modeled arcs of Figure 5 on the dynamic spectra observed by Voyager 2 on July 6-7, 1979 (upper), and July 3, 1979 (lower).

The upper panel is an example of an Io-dependent source A event (the phase of Io is  $240^\circ$  when the longitude is  $212^\circ$ ). The lower panel is an example of an Io-dependent source C event centered around  $330^\circ$  (Io phase is  $240^\circ$  at a longitude of  $329^\circ$ ).

Fig. 7. A demonstration that the arcs plotted in Figure 5 are homologous.  $\bar{f} \equiv (f - 1)/(f_{\max} - 1)$  is plotted versus  $\bar{\lambda} = (\lambda_{\max} - \lambda)/(\lambda_{\max} - \lambda_{\min})$ . The selected arcs are indicated on Figure 5 as dashed curves and are derived from field lines that cross the equatorial plane at  $\lambda = 160^\circ, 220^\circ$  and  $330^\circ$ .

Fig. 8. Similar to Figure 5, except that  $\psi_{\min} = 45^\circ$ . The resulting arc curvature is similar to that observed for the lesser arc patterns.

Fig. 9. A superposition of the modeled arcs shown in Figure 8 on a series of vertex-early lesser arcs observed by Voyager 2 on July 7, 1979.

Fig. 10. An attempt at modeling the early source (B) by setting  $\psi_{\min} = 73^\circ$ . In addition, here  $w = 2$  in the definition of  $f_v$ . Only the northern hemisphere vertex-early pattern is shown.

Fig. 11. A superposition of the modeled arcs of Figure 10 on an Io-dependent source B event observed July 7, 1979, by Voyager 2.

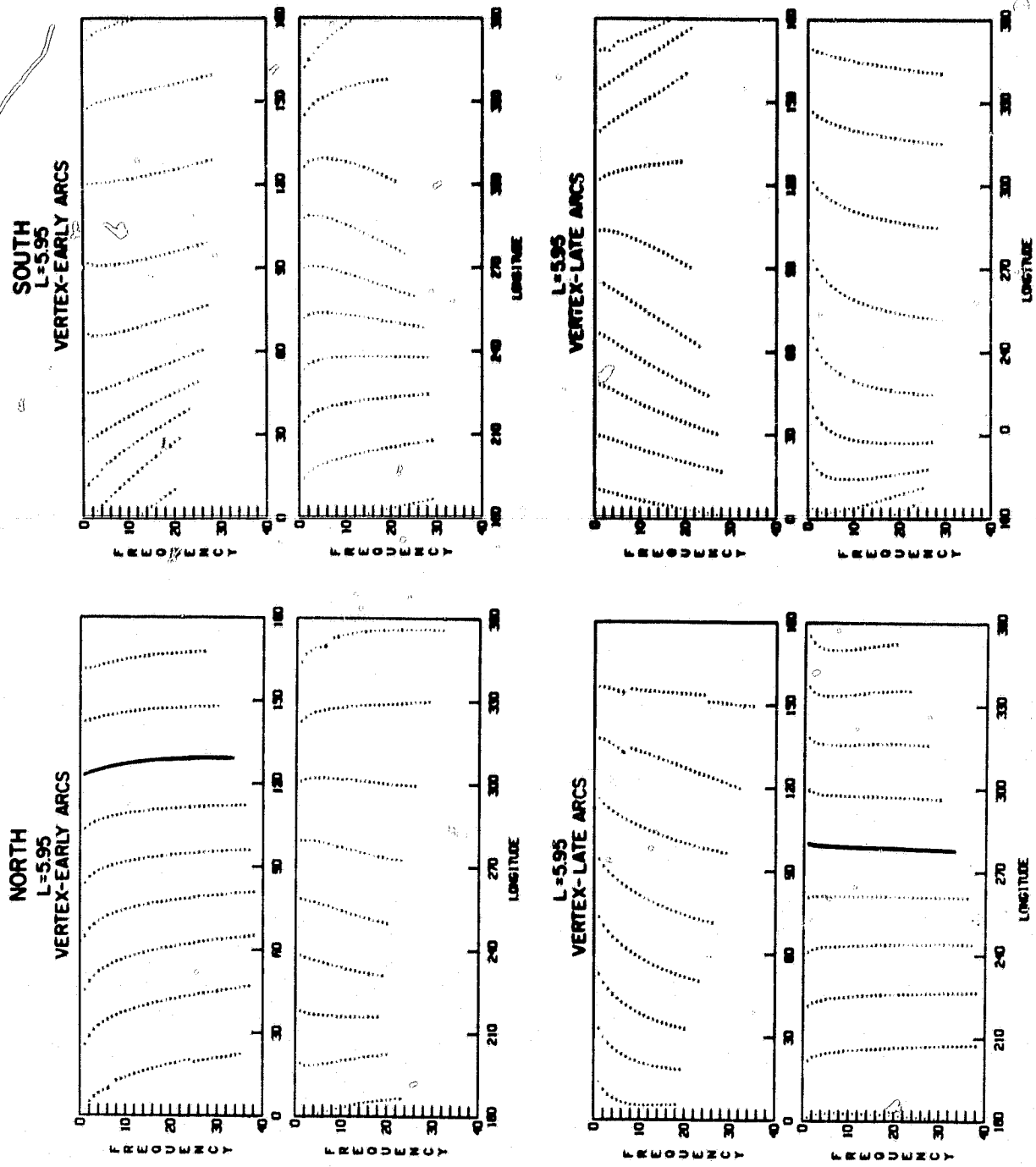


Figure 1

L=2.00 NORTH  
VERTEX-EARLY ARCS

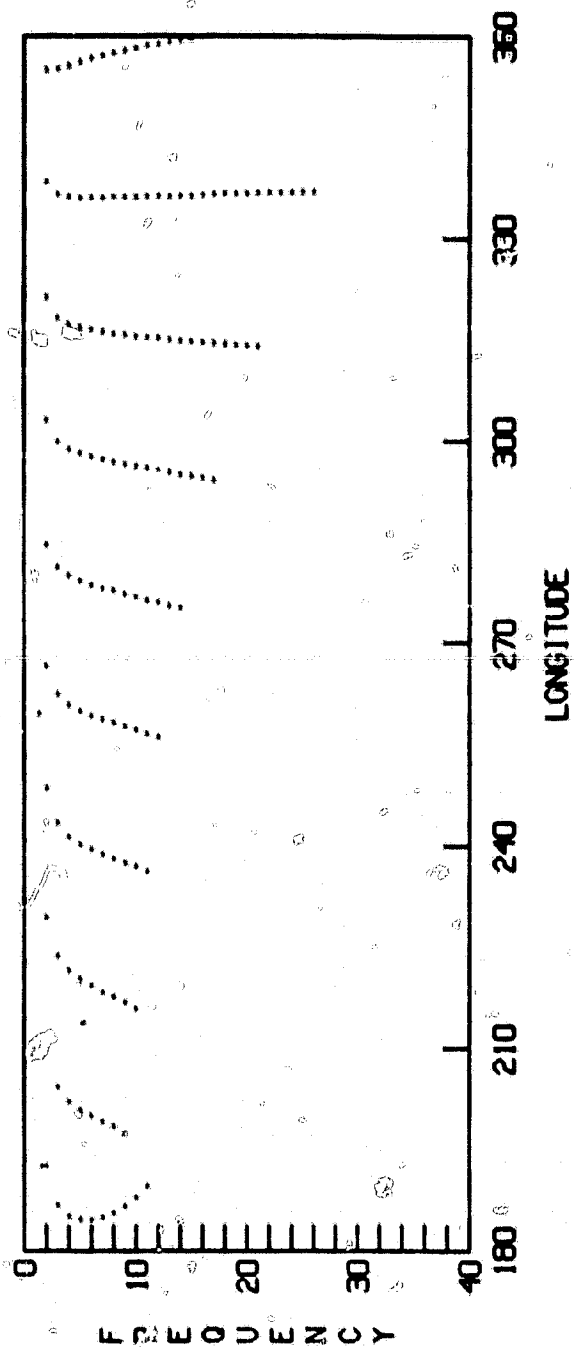
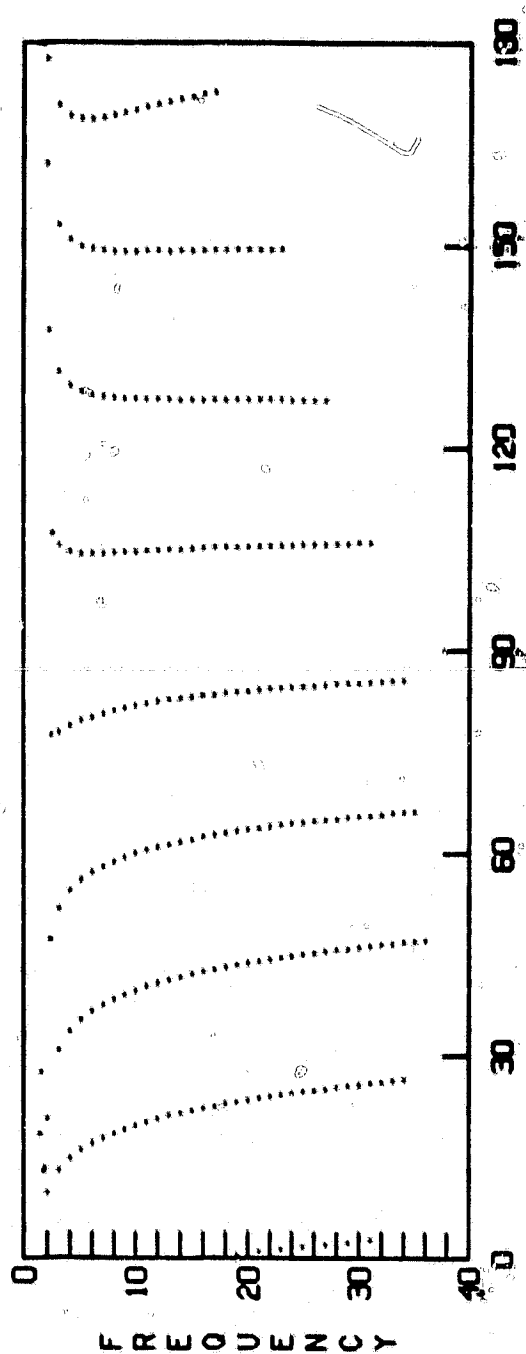


Figure 2



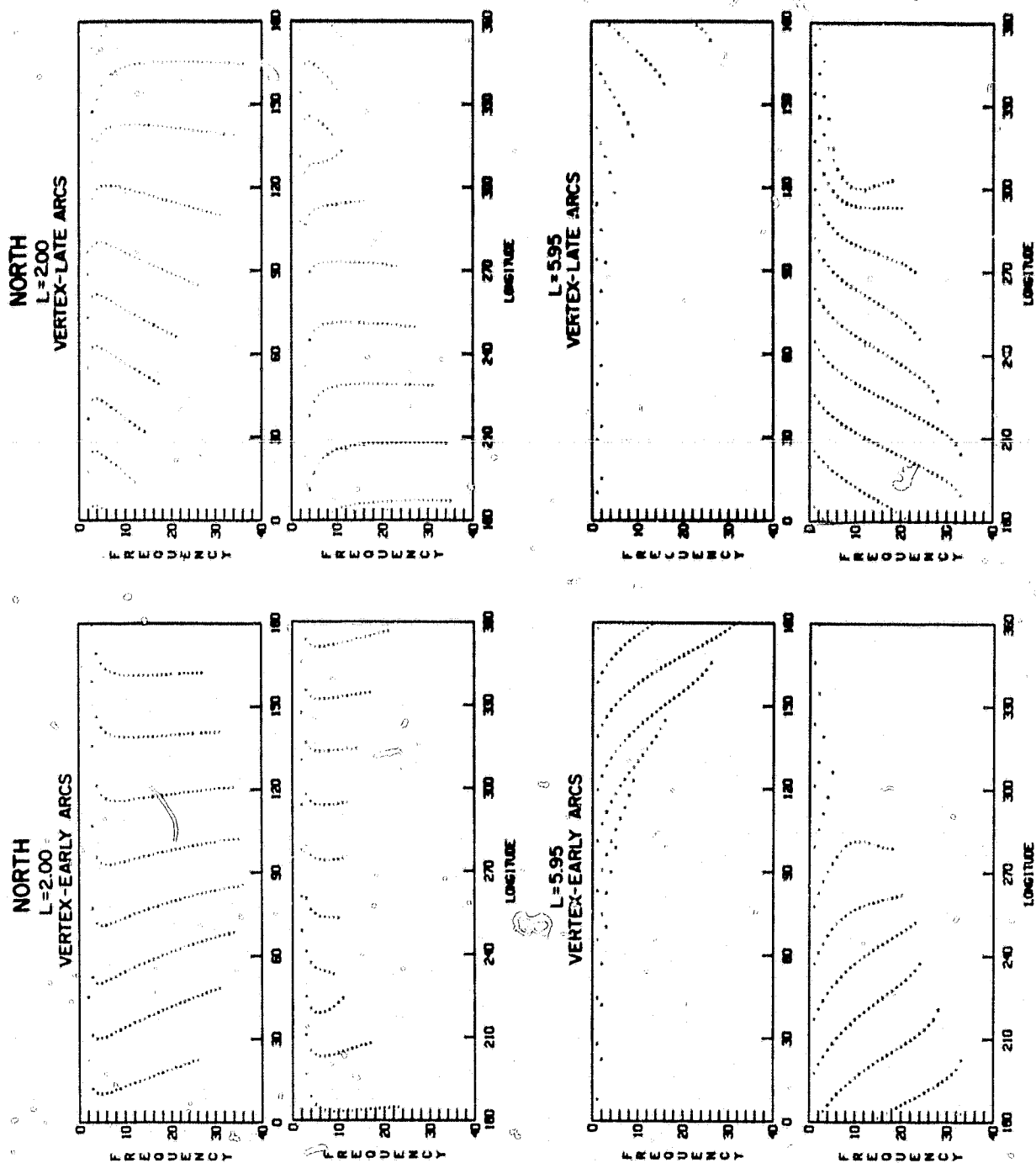


Figure 3

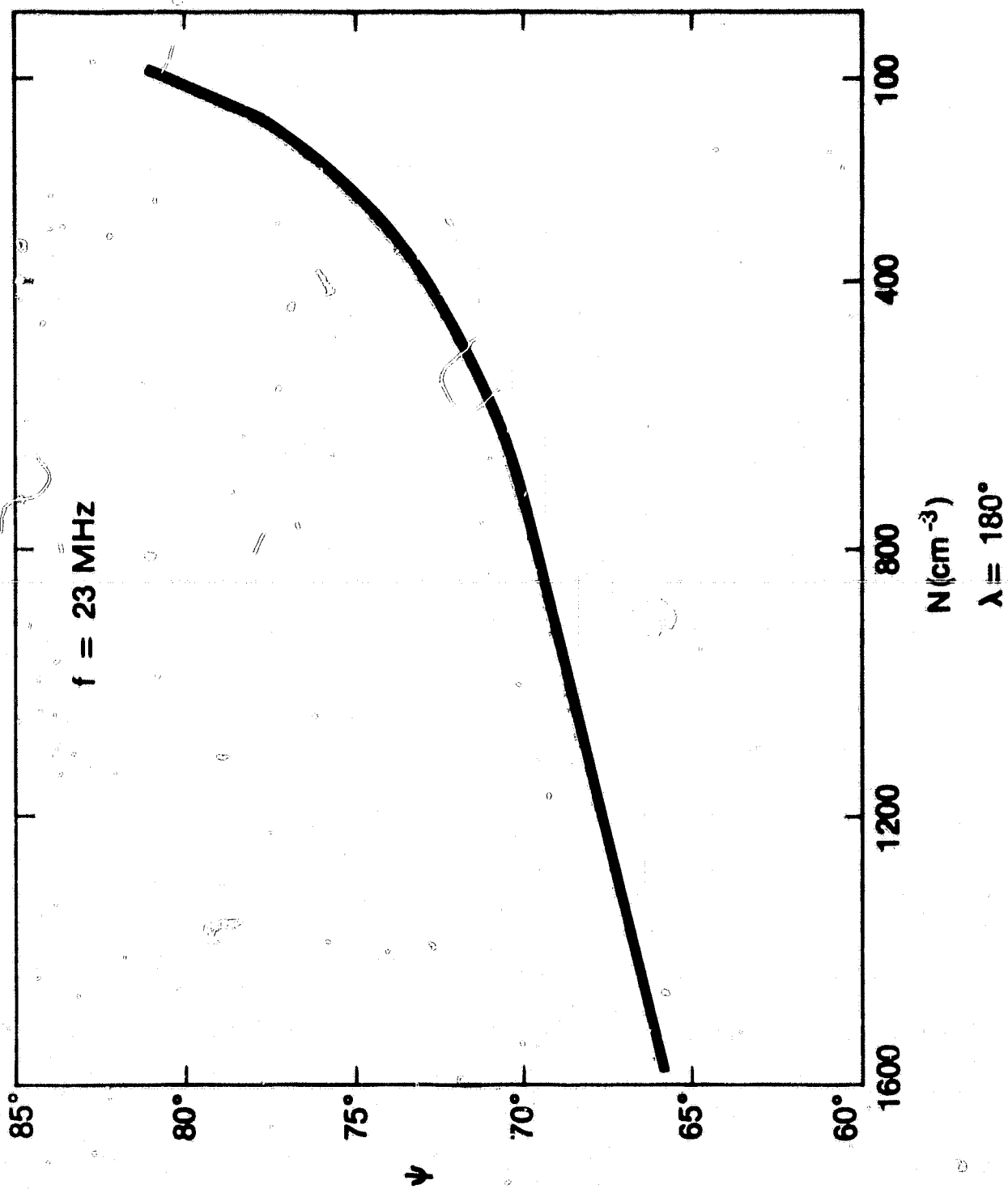


Figure 4

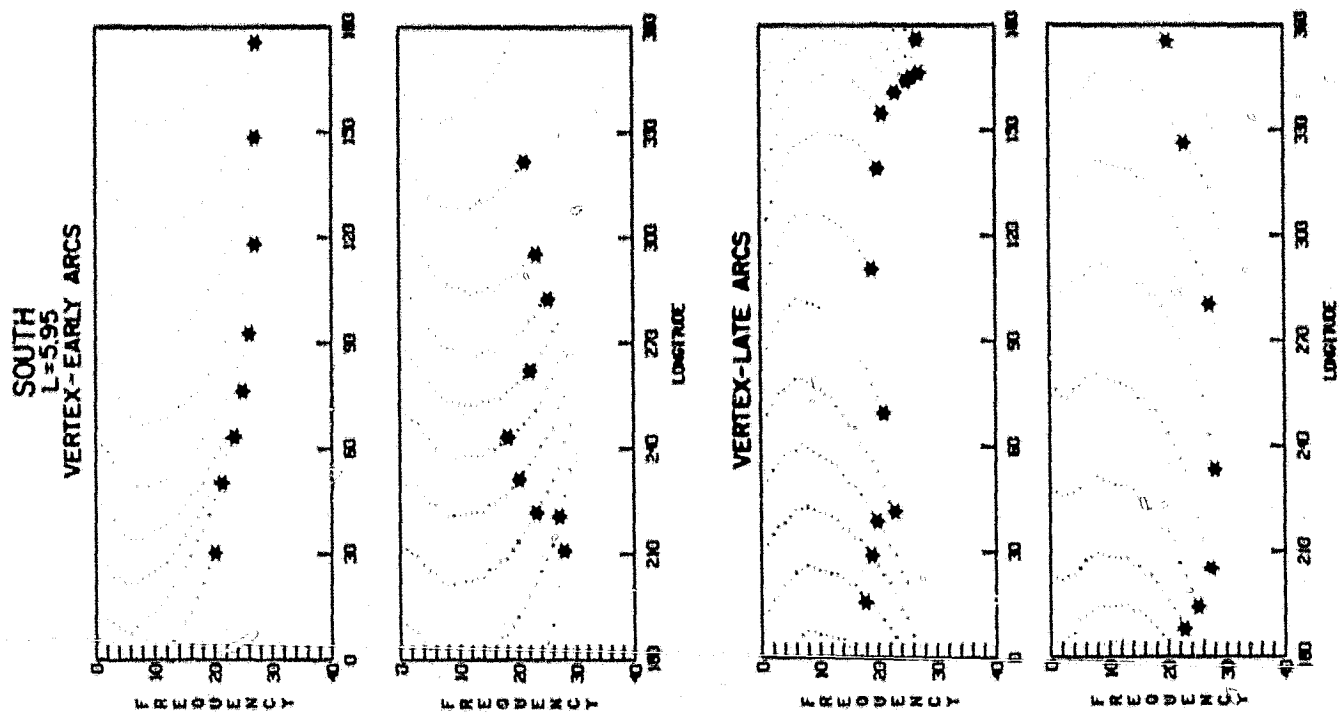
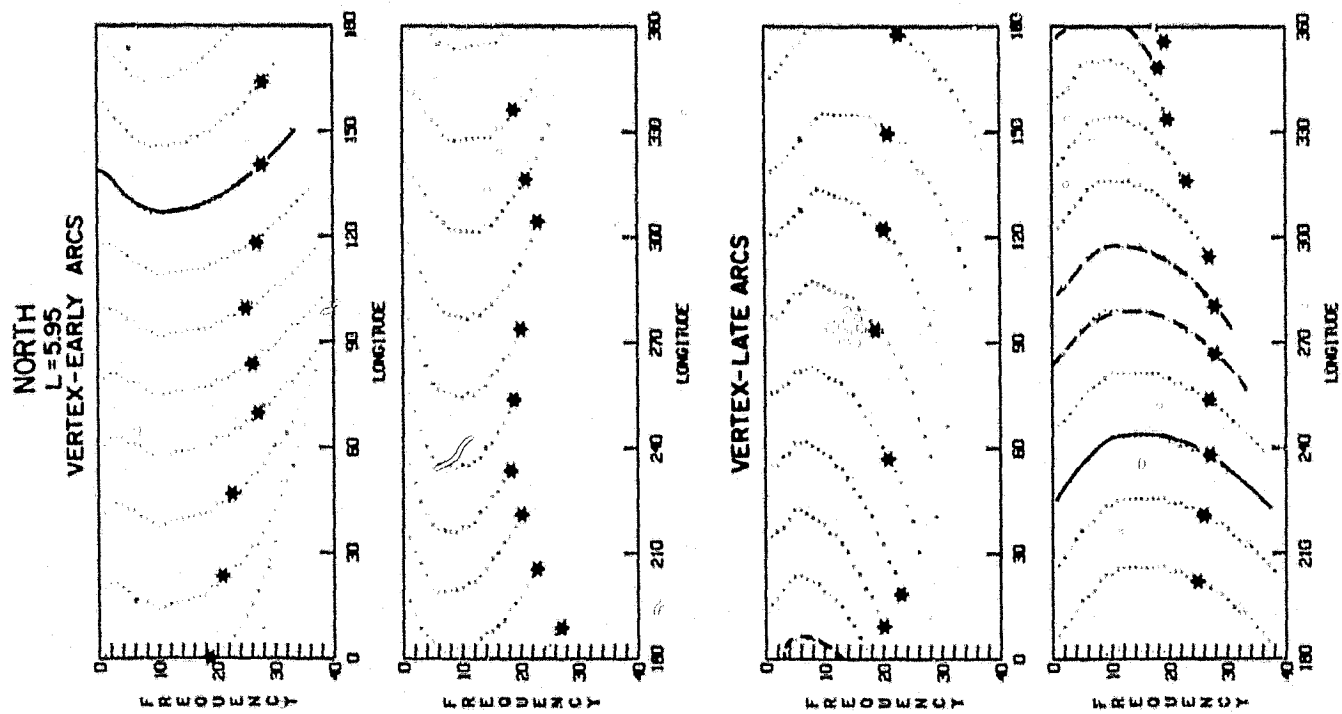


Figure 5

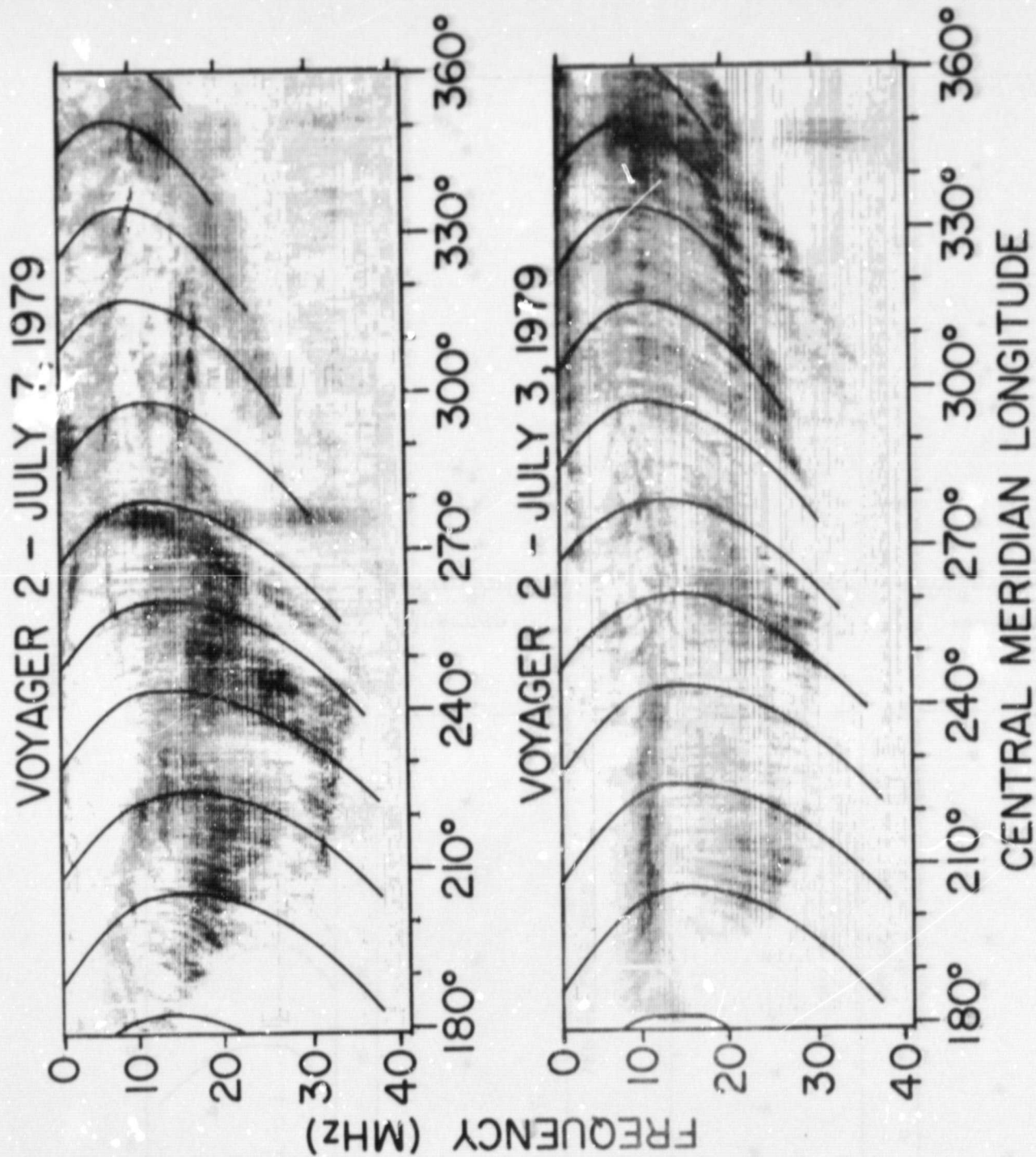


Figure 6

ORIGINAL PAGE IS  
OF POOR QUALITY

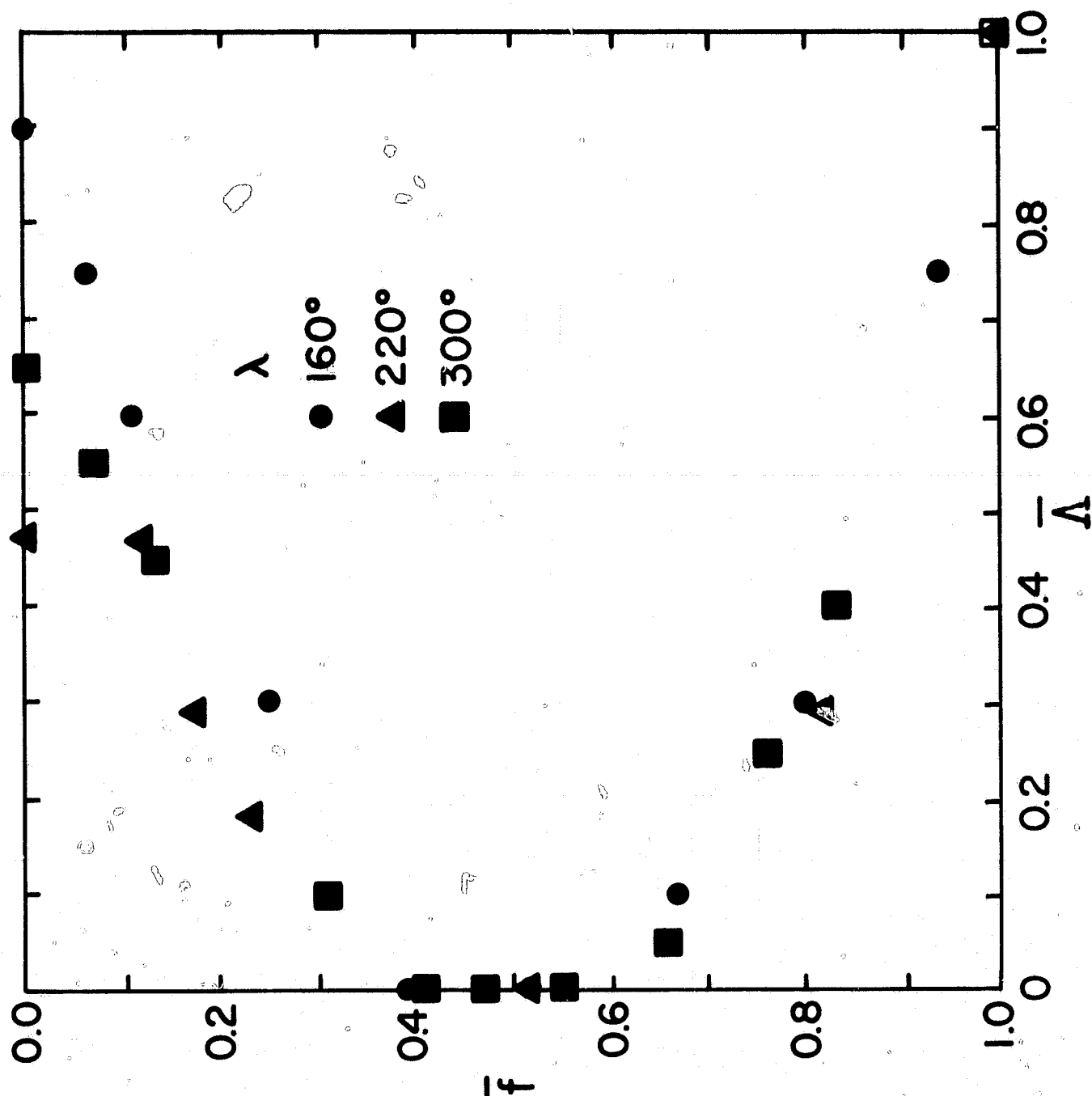
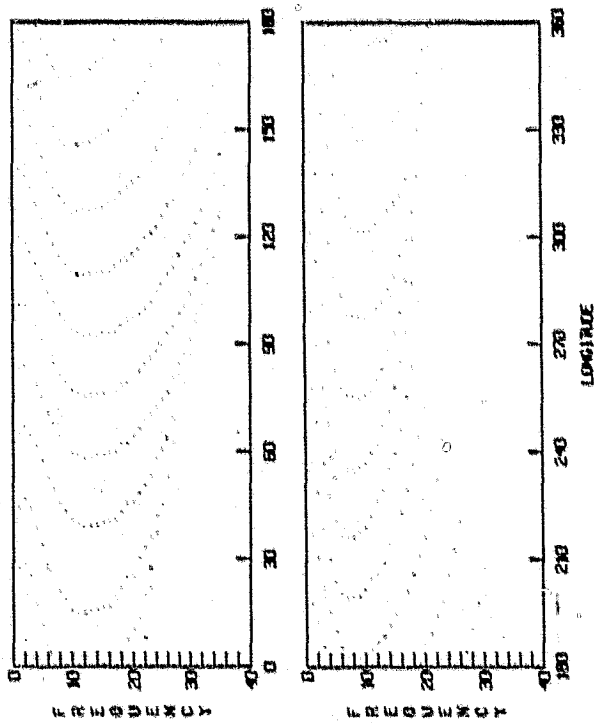
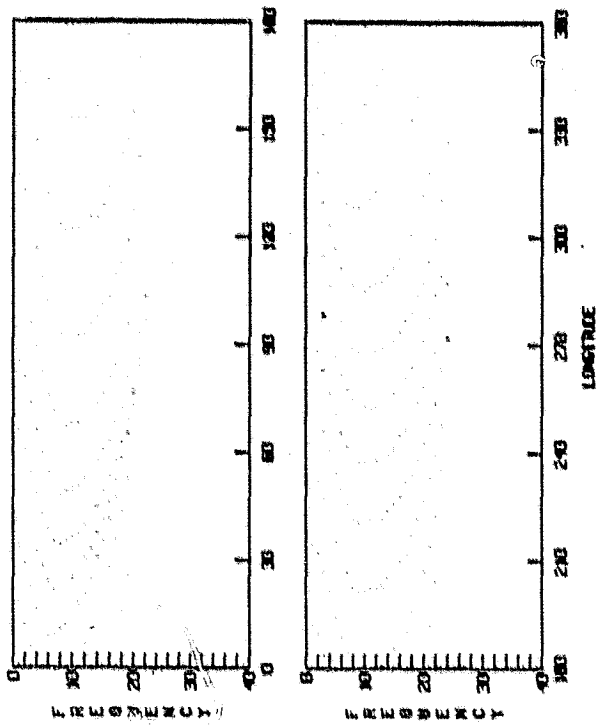


Figure 7

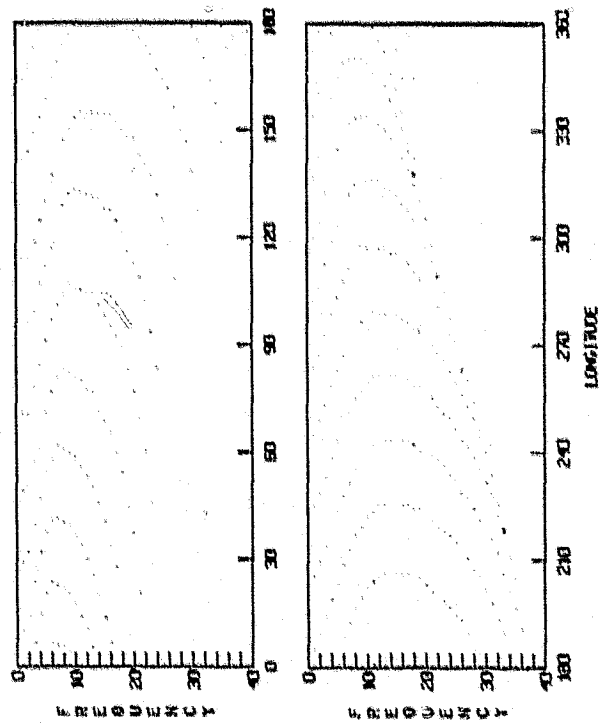
**NORTH**  
**L=5.95**  
**VERTEX-EARLY ARCS**



**SOUTH**  
**L=5.95**  
**VERTEX-EARLY ARCS**



**VERTEX-LATE ARCS**



**VERTEX-LATE ARCS**

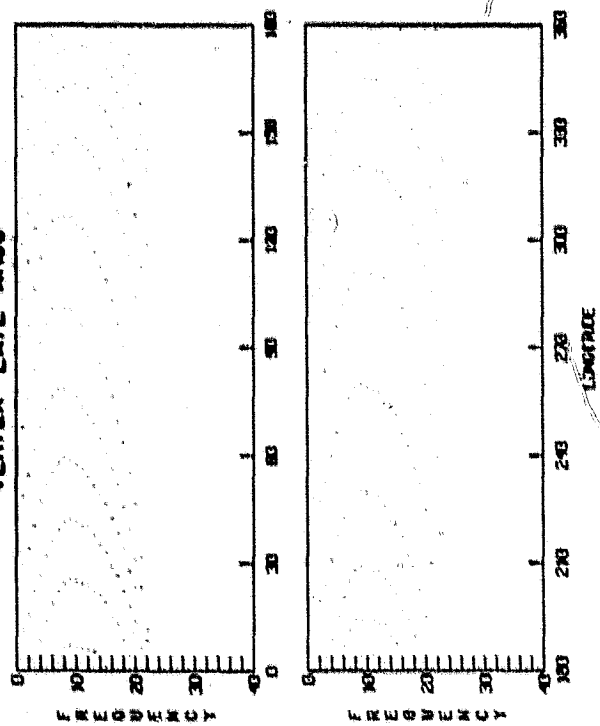
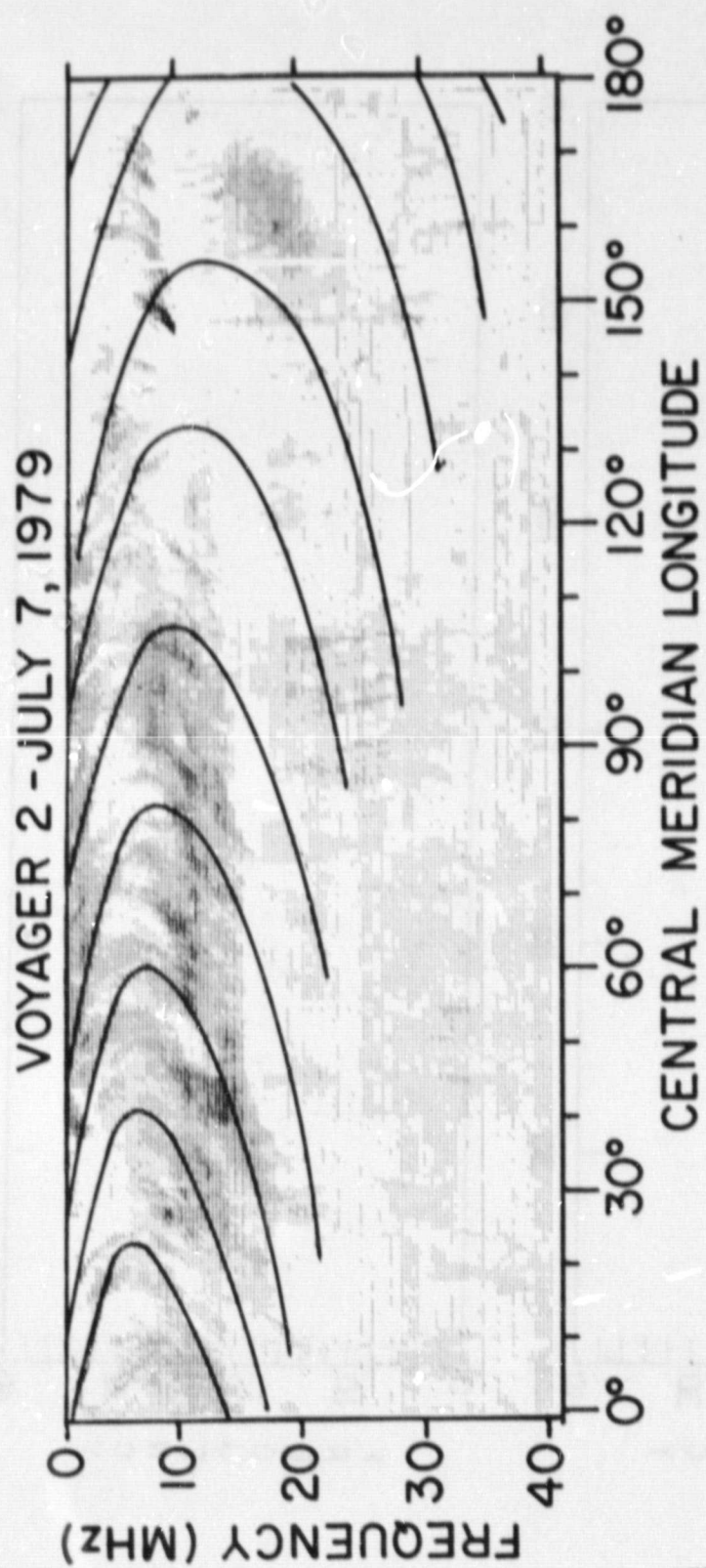


Figure 8



ORIGINAL PAGE 1  
OF POOR QUALITY

Figure 9

NORTH  
L = 5.95  
VERTEX-EARLY ARCS

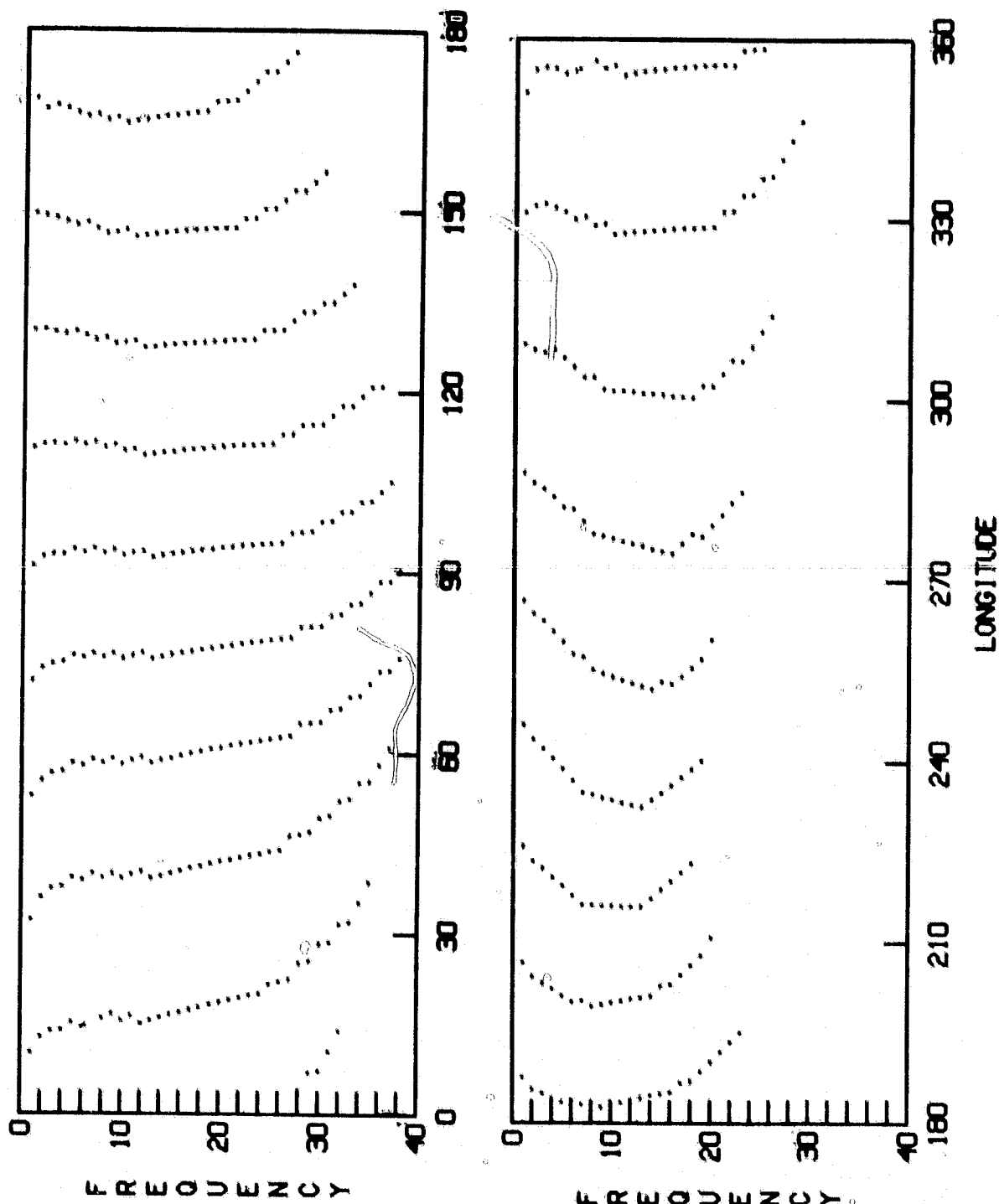


Figure 10



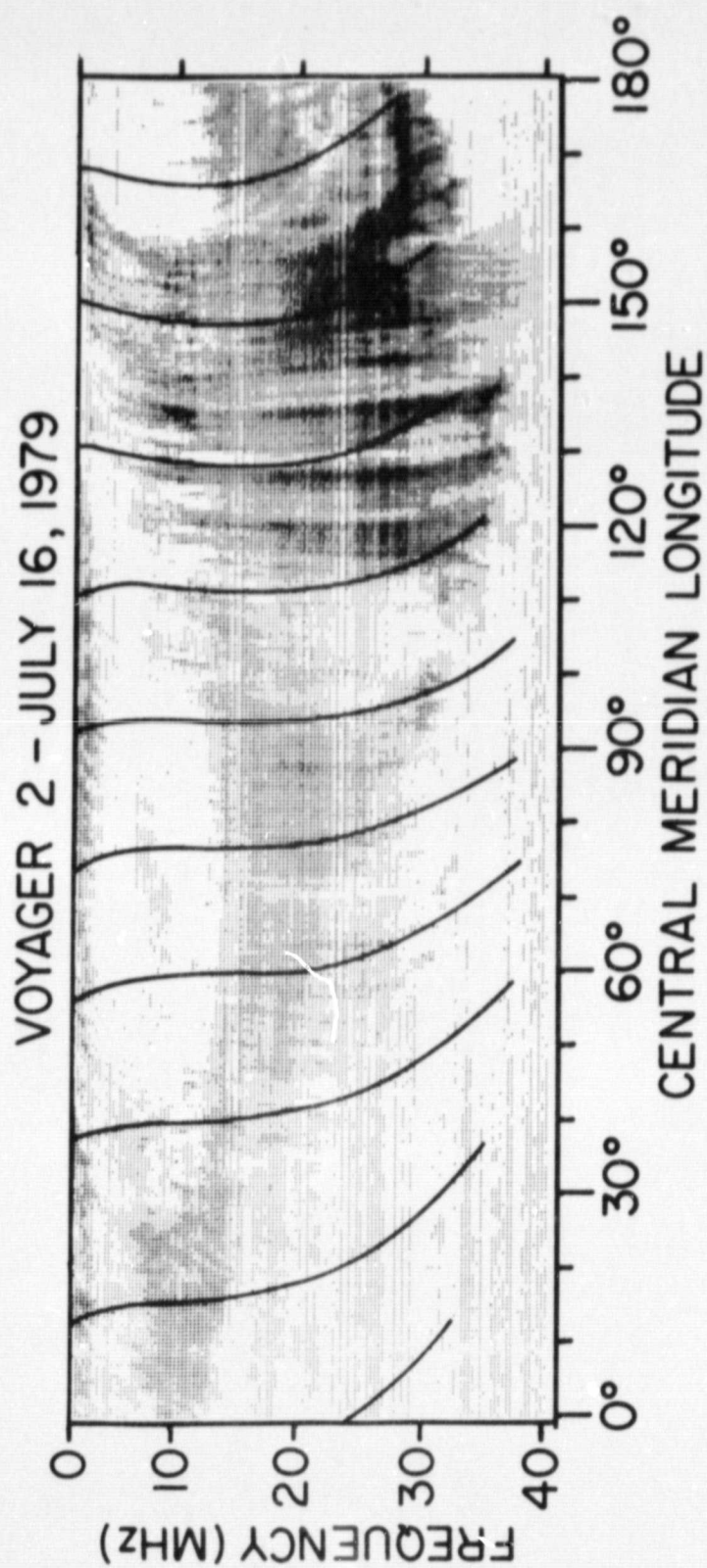


Figure 11

ORIGINAL PAGE IS  
OF POOR QUALITY